

Stochastic Dynamics for Video Infilling

Qiangeng Xu

qiangenx@usc.edu
University of Southern California

Hanwang Zhang

hanwangzhang@ntu.edu.sg
Nanyang Technological University

Weiyue Wang

weiyuewa@usc.edu
University of Southern California

Peter N. Belhumeur

belhumeur@cs.columbia.edu.com
Columbia University

Ulrich Neumann

uneumann@usc.edu
University of Southern California

Abstract

In this paper, we introduce a stochastic generation framework (SDVI) to infill long intervals in video sequences. To enhance the temporal resolution, video interpolation aims to produce transitional frames for a short interval between every two frames. Video Infilling, however, aims to complete long intervals in a video sequence. Our framework models the infilling as a constrained stochastic generation process and sequentially samples dynamics from the inferred distribution. SDVI consists of two parts: (1) a bi-directional constraint propagation to guarantee the spatial-temporal coherency among frames, (2) a stochastic sampling process to generate dynamics from the inferred distributions. Experimental results show that SDVI can generate clear and varied sequences. Moreover, motions in the generated sequence are realistic and able to transfer smoothly from the referenced start frame to the end frame.

Introduction

Video temporal enhancement is generally achieved by synthesizing frames between every two consecutive frames of a video. To our best knowledge, most studies (Meyer et al. 2018; Jiang et al. 2017) focus on interpolating videos with frame rate above 20 fps. The intervals between frames of these videos are short-term and suitable for interpolation methods. Instead, our study focuses on the **long-term interval infilling** for videos with frame rate under 3 fps. The applications of the study could be applied on low frame rate videos recorded by any camera with limited memory, storage, network bandwidth or low power supply (e.g., outdoor surveillance devices and webcam with an unstable network).

In Figure 1, conditioned on frame 7 and 8, the interpolation for a short-term interval generates transitional frames containing similar content. However, infill a long-term interval (from frame 8 to 12) with a synthesizing sequence requires to generate motion dynamics and varying content.

Figure 2 illustrates the stochastic nature of the long-term intermediate sequence. We observe the following two phenomena: (1) Compared with scenario 1, since both the interval length and the difference between the two reference frames are larger, the uncertainties and randomness in the

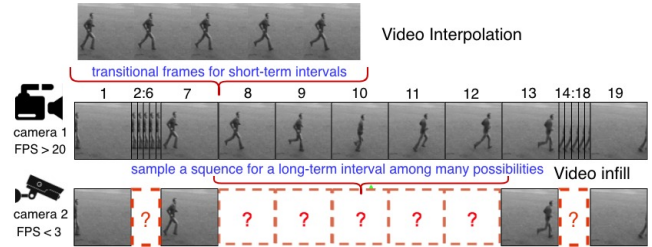


Figure 1: Task formulation: Camera 1 captures frames 1 to 19. Interpolation aims to generate 5 frames between frame 7 and 8. A low frame rate camera 2 can only capture frame 1, 7, 13 and 19 of the camera 1. Video infilling focuses on generating the intermediate dynamic sequence for camera 2 (a plausible sequence may be frame 8 to 12 of camera 1).

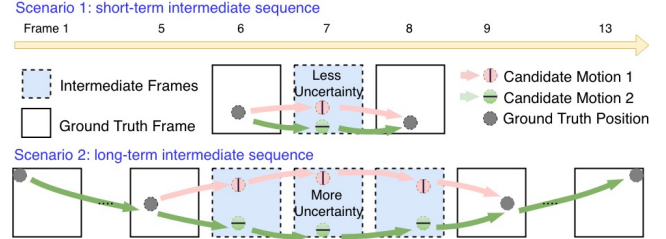


Figure 2: The difference of the stochasticity between short-term and long-term intervals: The camera in scenario 1 can capture every other frame and the camera in scenario 2 captures 1 frame for every 4 frames. The red and the green trajectories indicate two possible candidate motions in each scenario.

long-term interval is greater. (2) Taken frame 5 and 9 as references, both candidate motions in sequence 6 to 8 are possible. If we also add frame 1 and 13 as references, only motion 2 (the green trajectory) is plausible. Consequently, utilizing long-term information (frame 1 and 13 in Figure 2) can benefit the dynamics inference by eliminating uncertainties.

Most video interpolation methods (Niklaus and Liu 2018; Liu et al. 2017) rely on estimating the short-term pixel movements. While this approach falls short of long-term frame synthesis, recent video prediction models (Wichers et al. 2018; Denton and Fergus 2018) can generate the long-

term future with explicit motion modeling. In this paper, we model the motion dynamics in the same manner as the video prediction. The task has two major challenges: **1.** Unlike the video prediction, the temporal layout of our input is bi-directional with temporal gaps. No existing model is applicable; **2.** Interpolation requires coherency between the generated sequence and reference frames from both directions. To solve these challenges, we introduce a module *RBCovLSTM*, a multi-layer bi-directional ConvLSTM with residual connections between adjacent layers. To solve the long-term infilling task in Figure 1, we expose extended reference frames both from the past (frame 1 and 7) and the future (frame 13 and 19) to the *RBCovLSTM*. The dynamics from both sides are gradually propagated to the middle steps and create dynamic constraint vectors to guide the inference. These constraint vectors play significant roles to enforce the temporal coherency.

To model the stochasticity of the dynamics, we propose a stochastic generation model. The model first takes two reference frames and the extended reference frames to extract the dynamic features. Then we use the *RBCovLSTM* to create constraint vectors. At each step, a distribution is inferred conditioned on a constraint vector, and the dynamics generated previously. Then we sample the dynamics change from this distribution and synthesize a new frame. We design our objective function by optimizing a variational lower bound (see). SDVI stands out among previous studies on 4 datasets. We also infill the segments of a real-world video (2fps) and connect them to create the entire video with 16fps. (See the video web page in the supplemental material). To summarize, our contributions are:

- A stochastic model is proposed to generate long-term intermediate sequences. To the best of our knowledge, it is the first stochastic approach to solve the video infilling task, and the first model explicitly utilizes the extended reference frames away from the interval.
- A module *RBCovLSTM*(see) is introduced to enforce spatial-temporal coherency.
- A movement weight mask (see) is applied to help generate dynamics against the stale content.
- A metric LMS (see) is proposed to evaluate the sequence temporal coherency.

Related Works

Most studies of video interpolation (Ilg et al. 2017; Jiang et al. 2017) focus on generating high-quality intermediate frames in a short-term interval. Since we focus on long-term sequence infilling, our framework adopts long-term dynamics modeling. Therefore we also refer to the studies of video prediction which have explored this area from various perspectives.

Video Interpolation

Video interpolation generally has three approaches: optical flow based interpolation, phase-based interpolation, and pixels motion transformation. Optical flow based methods (Herbst, Seitz, and Baker 2009; Yu et al. 2013; Ilg et al. 2017) require an accurate optical flow inference. However,

the optical flow estimation is known to be inaccurate for a long time interval. Estimation of the motion dynamics becomes a more favorable option. The phase-based methods such as (Meyer et al. 2015) modify the pixel phase to generate intermediate frames. Although the strategy of propagating phase information is elegant, the high-frequency and drastic changes cannot be properly handled. The inter-frame change will be more significant in our long-term setting. Currently studies (Liu et al. 2017; Niklaus, Mai, and Liu 2017b; Jiang et al. 2017) use deep learning methods to infer the motion flows between the two frames. By far, this branch of approaches achieves the best result and has the potential to solve our task. In our evaluation, we use SepConv (Niklaus, Mai, and Liu 2017a) and SuperSloMo (Jiang et al. 2017) as comparisons.

Deterministic Video Prediction

The mainstream video prediction methods take short consecutive sequences as input and generate deterministic futures by iteratively predicting next frame. (Vondrick, Pirsavash, and Torralba 2016; Mathieu, Couprie, and LeCun 2015) use a convolutional network to generate each pixel of the new frame directly. Studies such as (Srivastava, Mansimov, and Salakhudinov 2015; Finn, Goodfellow, and Levine 2016) use a recurrent network to model the dynamics change and improve the result drastically. (Xingjian et al. 2015) introduces ConvLSTM, which has been proved to be powerful in spatial sequence modeling. (Villegas et al. 2017; Denton and others 2017) propose to model the content and the dynamics independently to reduce the workload for the networks. (Tulyakov et al. 2017; Villegas et al. 2017) incorporate GANs (Goodfellow et al. 2014) into their model and improve the quality. Notably, two of the generative models (Lu, Hirsch, and Schölkopf 2017) and (Cai et al. 2017) can also conduct video completion. However both methods, due to their forward generation mechanism, cannot hold the coherency between the last frame and the generated sequence. SDVI adopts the decomposition of the motion and the content, uses the ConvLSTM in the motion inference and iteratively generates the frame. However, we don't use GANs since our study focuses more on dynamics generation. We also compare SDVI with FSTN in (Lu, Hirsch, and Schölkopf 2017), a prediction model that can also handle video infilling.

Stochastic Video Generation

After (Babaeizadeh et al. 2017; Henaff, Zhao, and LeCun 2017) shows the importance of the stochasticity in video prediction, later studies such as (Lee et al. 2018; Denton and Fergus 2018) also conduct the prediction in the form of stochastic sampling. The stochastic prediction process consists of a deterministic distribution inference and a dynamic vector sampling. We also adopt this general procedure. Since SVG-LP introduced in ((Denton and Fergus 2018)) is one of the state-of-the-art models and very related to our study, we use the SVG-LP to compare with SDVI.

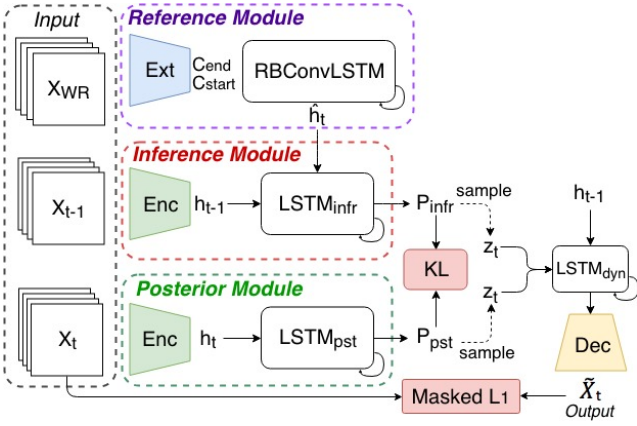


Figure 3: Training of SDVI: All green *Encoder* modules share the same weights. The blue module denotes the *Extractor* and the yellow module denotes the *Decoder*. The Reference module creates dynamic constraint \hat{h}_t for each step. At step t , the Inference module takes X_{t-1} and \hat{h}_t , while the Posterior module takes X_t . The Inference module and the Posterior module will produce different z_t and therefore different output frames \tilde{X}_t^{infr} and \tilde{X}_t^{pst} .

Methods

Following the standard input setting of temporal super-resolution, we formulate our task as follows: For a sequence \mathbf{X} , only one frame out of every u frames is captured. SDVI infills the sequence $X_{S+1:T-1}$ between reference frames X_S and X_T . In Figure 1, X_S and X_T are frame 7 and 13. $X_{S+1:T-1}$ is the sequence from frame 8 to 12. We also use additional frames (frame 1 and 19) as extended references.

$$\underbrace{X_{S-e \times u}, \dots, X_{S-u}}_{\text{extended reference frames}}, \underbrace{X_S, X_{S+1:T-1}}_{\text{our target}}, \underbrace{X_T, X_{T+u}, \dots, X_{T+e \times u}}_{\text{extended reference frames}}$$

We use X_S , X_T and extended reference frames as the full reference frame set, denoted as “window of reference” \mathbf{X}_{WR} . A hyper parameter e denotes the number of ground truth frames on each side of the extended references. We will show the impact of these information in the ablation study. Different from existing methods, SDVI uses $P(X_{S+1:T-1} | \mathbf{X}_{WR})$ instead of $P(X_{S+1:T-1} | X_S, X_T)$. As illustrated in Figure 3, SDVI consists of 3 major modules: reference, inference and posterior modules. The Reference module helps to propagate the constraint to each time step. The Inference and the Posterior module work together to train the stochastic dynamics generation. We list the notations as follows:

- * X_t : Ground truth frames at time t .
- * C_{start} and C_{end} : Momentum vectors extracted from \mathbf{X}_{WR} , used as initial cell states for *RBCConvLSTM*.
- * h_t : The dynamic feature vector extracted from a ground truth frame by the *Encoder*: $h_t = Enc(X_t)_{dyn}$. $h_{S:T}$ is the sequence of the dynamic features from S to T .
- * \hat{h}_t : The dynamic constraint vector for the step t . We have $\hat{h}_{S:T} = RBCConvLSTM(X_{WR}, X_S, X_T)$

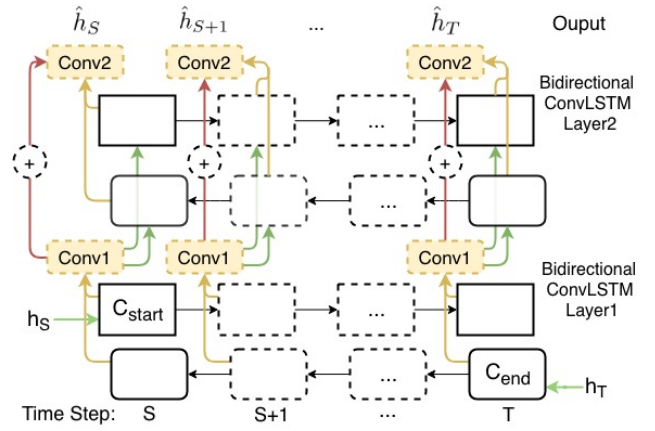


Figure 4: A two layers RBCConvLSTM: The initial cell states of the first layer are assigned as C_{start} and C_{end} . h_S and h_T are taken as inputs. Combined with the residuals (red arrow), each layer’s outputs would go through a convolution module and become the input to the next layer. All the convolution modules in the same layer share the same weights.

- * P_{infr} and P_{pst} : The simplified notations of $P_{infr}(z_t | X_{S:t-1}, \mathbf{X}_{WR})$ and $P_{pst}(z_t | X_{S:t})$. The distributions of the dynamics change generated by the Inference and the Posterior module. (Details in)
- * z_t : The dynamics change vector on time step t . z_t^{infr} is sampled from P_{infr} and z_t^{pst} is sampled from P_{pst} .
- * \tilde{X}_t : The frame generated on step t . The Posterior and the Inference module generate \tilde{X}_t^{pst} and \tilde{X}_t^{infr} respectively.

Reference Module

The Reference module includes an *Extractor* and a *RBCConvLSTM*. Given all the frames in \mathbf{X}_{WR} , the *Extractor* learns the momentum and output two vectors C_{start} and C_{end} . The *RBCConvLSTM* is a residual bi-directional ConvLSTM. The first layer of *RBCConvLSTM* uses C_{start} as the initial state of the forward cell and C_{end} for the backward cell. We also input h_S to the forward cell and h_T to the backward cell. For each step t , *RBCConvLSTM* outputs a dynamic constraint vector \hat{h}_t . The whole dynamic constraint sequence has a conditional distribution $P(\hat{h}_{S:T} | \mathbf{X}_{WR})$.

RBCConvLSTM Our Reference module is essentially a sequence completion model. We need to transfer an incomplete sequence $h_S, \mathbf{0}, \dots, h_T$ to a complete sequence $\hat{h}_S, \hat{h}_{S+1}, \dots, \hat{h}_T$. Stacking multiple layers of RNN is a common practice for such task. In our model, input features to the bottom layer $h_S, \mathbf{0}, \dots, h_T$ share the same space with the output features $\hat{h}_{S:T}$ of the top layer. Inspired by (He et al. 2015), we add an residual connection between each two layers to elevate the bottom features directly to the top. In the end, RBCConvLSTM combines all the three structures: the ConvLSTM, the bi-directional RNN and the residual connections. Its structural details are shown in Figure 4.

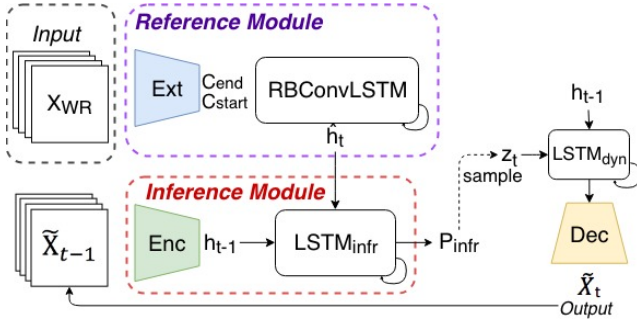


Figure 5: Inference of SDVI: Without ground truth frame X_{t-1} , the generated frame \tilde{X}_{t-1} serves as the input to the Inference module on step t .

Inference Module

We extract a dynamic vector h_t from each ground truth frame X_t . At time step t , the $LSTM_{infr}$ takes the h_{t-1} and the dynamic constraint vector \hat{h}_t , then infers a distribution P_{infr} of the possible dynamic changes. This module resembles the prior distribution learning of stochastic prediction since the hidden vector h_t is not exposed to the network at step t . Because we also refer to the \hat{h}_t which is conditioned on the \mathbf{X}_{WR} , the distribution becomes $P_{infr}(z_t | X_{S:t-1}, \mathbf{X}_{WR})$.

Posterior Module

A generated sequence $\tilde{X}_{S+1:T-1}$ can still be valid even it shows different dynamics than the ground truth $X_{S+1:T-1}$. Therefore our model need to acquire a target distribution P_{pst} for step t , so the Inference module can be trained by matching P_{infr} to the target. Here we expose the frame X_t to the Posterior module. Then the dynamic information on step t can be passed to the $LSTM_{pst}$, so it can generate a posterior distribution $P_{pst}(z_t | X_{S:t})$ for $P_{infr}(z_t | X_{S:t-1}, \mathbf{X}_{WR})$ to match.

Training

From P_{pst} , we can sample a dynamics change vector z_t^{pst} . Along with the dynamics vector h_{t-1} from the step $t-1$, the $LSTM_{dyn}$ can generate a motion representation. Finally, the *Decoder* combines the motion representation with content residuals $Enc(X_S, X_T)_{ctn}$ and generates the \tilde{X}_t^{pst} . Separately, we also sample a vector z_t^{infr} from P_{infr} , and generate the \tilde{X}_t^{infr} in the same way. The training pipeline is shown in Figure 3.

Inference

Since the ground truth frames $X_{S+1:T-1}$ are not available during inference, we cannot obtain X_t at time t . Therefore we use only Inference module to sample z_t . The inference pipeline is shown in Figure 5. At each step, the generated frame \tilde{X}_t will serve as the input for both the $LSTM_{infr}$ and the $LSTM_{dyn}$ in the next step.

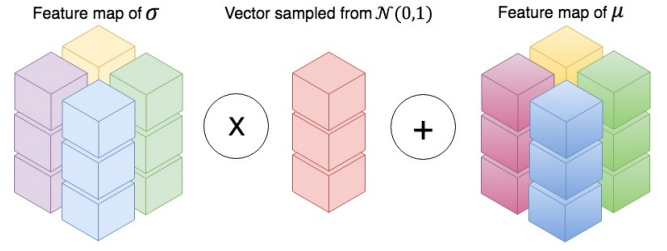


Figure 6: The sampled vector (in the middle) is applied on all locations.

Dynamic Spatial Sampling

In order to train P_{pst} and P_{infr} at t , we model them as Gaussian distributions $N_{pst}(\mu_t, \sigma_t)$ and $N_{infr}(\mu_t, \sigma_t)$, using the re-parameterization trick from (Kingma and Welling 2013). A Gaussian distribution can be mapped to any distribution through a sufficient complicated function (simulated by a part of our neural network). After inferring the μ_t and the σ_t , we will sample a vector from the Gaussian distribution. Different from (Denton and Fergus 2018), we consider a spatial vector as a stronger representation for the movement. Different locations in one frame may have different levels of stochasticity. Uniformly draw a sample following the same distribution everywhere will hinder the modeling (see SDVI non-spatial in Table 1). Consequently, we introduce a spatial sampling process (Figure 6). Instead of using vectors, we use spatial feature maps for μ_t and σ_t . To get the z_t , we multiply the sampled vector on each location of σ_t , then add the μ_t on the product.

Loss Function

Reconstruction Loss To make the \tilde{X}_t^{pst} reconstruct real X_t , we introduce a pixel loss $L_1(X_t, \tilde{X}_t^{pst})$. We also observe that imposing a pixel loss to the \tilde{X}_t^{infr} after the P_{infr} getting stable can further improve the video quality during inference.

KL Divergence Loss The $P_{pst}(z_t | X_{S:t})$ carries the dynamics change from the h_t to reconstruct the X_t . Since we use only the Inference module during inference, the $P_{infr}(z_t | X_{S:t-1}, \mathbf{X}_{WR})$ needs to predict the dynamics change alone. Therefore, we also add two KL divergences between $P_{infr}(z_t | X_{S:t-1}, \mathbf{X}_{WR})$ and $P_{pst}(z_t | X_{S:t})$. Both the forward and the reverse KL-divergence of P_{infr} and P_{pst} achieve the minimum when the two distributions are equal. However, according to (Fox and Roberts 2012), since $D_{KL}(P_{pst} || P_{infr})$ is sampled on P_{pst} , it will penalize more when P_{pst} is large and P_{infr} is small. Therefore this term will lead to a P_{infr} with higher diversity. On the other hand, $D_{KL}(P_{infr} || P_{pst})$ will make the inference more accurate when P_{infr} has large value. To better serve our task, we decide to keep both terms to strike a balance between accuracy and diversity.

Full Loss Overall, our final objective is to minimize the combined loss:

$$L_C = \sum_{t=S+1}^{T-1} [\beta \cdot L_1(X_t, \tilde{X}_t^{pst}) + (1 - \beta) \cdot L_1(X_t, \tilde{X}_t^{infr}) + \alpha \cdot D_{KL}(P_{pst} || P_{infr}) + \gamma \cdot D_{KL}(P_{infr} || P_{pst})] \quad (1)$$

The β balances the posterior reconstruction and the inference reconstruction, while the α and the γ determines the trade-off between the reconstruction and the similarity of the two distributions. To show the effectiveness of these loss terms, we also compare the full loss (1) with a loss only composed of the term 1 and 3 (similar to the loss in (Denton and Fergus 2018)), shown as ‘‘SDVI loss term 1&3’’ in Table 1.

Theoretical Explanation To theoretically validate this loss function, we develop a variational lower bound which is inspired by the ELBO in (Kingma and Welling 2013). To maximize a sequence’s probability $P(\tilde{X}_{S:T})$. We can maximize the variational lower bound of its logarithm (See Appendix A in the supplemental material for details):

$$\sum_{t=S}^{T-1} \mathbb{E}_{Q(z_t)} \log P(\tilde{X}_t | \tilde{X}_{S:t-1}, z_{S:t}) - \int_z Q(z_{S:T}) \log \frac{Q(z_{S:T})}{P(z_{S:T})} \quad (2)$$

Since we are interested in maximizing $\log P(\tilde{X}_{S:T-1}^{infr})$, we can fit P_{pst} and P_{infr} into (2)’s $P(z_{S:t})$ and $Q(z_{S:t})$ and get (See Appendix B for deduction details):

$$\log P(\tilde{X}_{S:T-1}^{infr}) \geq \sum_{t=S}^{T-1} \left[\mathbb{E}_{P_{infr}(z_t)} \log P(X_t^{infr} | X_{S:t-1}^{infr}, z_{S:t}^{infr}) - D_{KL}(P_{infr}(z_t | X_{S:t-1}^{infr}, \mathbf{X}_{WR}) || P_{pst}(z_t | X_{S:t}^{pst})) \right] \quad (3)$$

However, if we only maximize the lower bound above, the $LSTM_{pst}$ will tend to ignore the information in X_t since it has not been exposed to $LSTM_{infr}$ on time step t . The $P_{infr}(z_t)$ and $P_{pst}(z_t)$ will degenerate to a convenient fixed value to lower the D_{KL} . Thus we also need to enforce the reconstruction of the Posterior Module and maximize $\log P(\tilde{X}_{S:T-1}^{pst})$. Similarly, we fit P_{infr} and P_{pst} into (2)’s $P(z_{S:t})$ and $Q(z_{S:T})$ to get its variational lower bound :

$$\log P(\tilde{X}_{S:T-1}^{pst}) \geq \sum_{t=S}^{T-1} \left[\mathbb{E}_{P_{pst}(z_t)} \log P(X_t^{pst} | X_{S:t-1}^{pst}, z_{S:t}^{pst}) - D_{KL}(P_{pst}(z_t | X_{S:t-1}^{pst}) || P_{infr}(z_t | X_{S:t-1}^{infr}, \mathbf{X}_{WR})) \right] \quad (4)$$

We can see in the loss function (1): loss term 1 helps increase the first term of (4). Loss term 2 aims to improve the first term of (3). And loss terms 3 and 4 penalizes the second terms in (3) and (4).

Movement Weight Mask We apply a movement weight mask to each location of the pixel loss. If a pixel value stays the same as the previous step, the weight is 1 on that location. Otherwise, we either set the weight to 0 if it’s a flickering pixel (determined by its isolation level) or set the weight

to $\eta > 1$ to penalize the moving region. This operation helps us (1) denoise the content changes, (2) encourage the dynamic learning to prevent the stale sequence generation. The mask is visualized in Figure 12.

Experiments

We first test SDVI on 3 datasets with stochastic dynamics: Stochastic Moving MNIST(SM-MNIST) (Denton and Fergus 2018) with random momentum after a bounce, KTH Action Database (Schuldt, Laptev, and Caputo 2004) for deformable objects and BAIR robot pushing dataset (Ebert et al. 2017) for sudden stochastic movements. We also compare with the interpolation models on a challenging real-world dataset, UCF101(?). An infilled sequence that is different from the ground truth (low SSIM and PSNR) is still valid if its dynamic pattern makes sense. Thus we introduce the last momentum similarity (LMS) calculated by the mean square distance between the optical flow from X_{T-1} to X_T and the optical flow from \tilde{X}_{T-1}^{infr} to X_T . We find LMS a good indicator of the video coherency since no matter how the dynamic being sampled, both the object’s position and speed should make a smooth transition to X_T . Three metrics are used for quantitative evaluation: structural similarity (SSIM), Peak Signal-to-Noise Ratio (PSNR), and LMS.

We compare our results with other state-of-the-art models: FSTN(Lu, Hirsch, and Schölkopf 2017), a deterministic generation model; SVG-LP(Denton and Fergus 2018), an advanced stochastic prediction model; and two high-performance interpolation models SepConv(Niklaus, Mai, and Liu 2017a) and SuperSloMo(Jiang et al. 2017). Since FSTN and SVG-LP are not designed to solve infilling task, we concatenate the representation of the last frame X_T to their dynamic feature maps in each step. Then the SVG-LP simulates SDVI without the Reference module, and the FSTN is equivalent to SDVI without the Reference and the Posterior module. Ablation studies are conducted by removing the spatial sampling or the extended reference frames in \mathbf{X}_{WR} . Due to SepConv’s limitation (can only interpolate sequence with the length of $2^n - 1$), all the following evaluations are under the generation of 7 intermediate frames (see Appendix E for results under more conditions). Following their instruction, we complete the training code of SepConv to train the model on all datasets. We can’t get the code of SuperSloMo. Thus we acquire the results from the authors of (Jiang et al. 2017). More video results for various settings (see the video web page), dataset details (Appendix D), network architectures and the training details (see Appendix C) can be found in the supplemental material.

Stochastic Moving MNIST (SM-MNIST)

Digits in SM-MNIST introduced by (Denton and Fergus 2018) will bounce off the wall with a random speed and direction. The uncertainties of the outcome after a bounce make it a challenging task for all methods. The Avg PSNR, SSIM and LMS over all test frames are shown in Table 1. We also plot the metric values averaging on each step in Figure 7. Figure 8 shows the qualitative evaluation for all comparisons. When the two digits in frames 8 and 16 having signif-

	SM-MNIST			BAIR			KTH			UCF101		
	PSNR	SSIM	LMS	PSNR	SSIM	LMS	PSNR	SSIM	LMS	PSNR	SSIM	LMS
SDVI full model	16.025	0.842	0.503	21.432	0.880	1.05	29.190	0.901	0.248	16.635	0.598	15.678
SDVI without 0 & 24	14.857	0.782	1.353	19.694	0.852	1.360	26.907	0.831	0.478	—	—	—
SDVI non-spatial	13.207	0.752	6.394	19.938	0.865	1.159	29.366	0.896	0.276	—	—	—
SDVI loss term 1&3	15.223	0.801	0.632	19.456	0.849	1.277	28.541	0.854	0.320	—	—	—
SVG-LP	13.543	0.741	5.393	18.648	0.846	1.891	28.131	0.883	0.539	—	—	—
FSTN	14.730	0.765	3.773	19.908	0.850	1.332	29.431	0.899	0.264	—	—	—
SepConv	14.759	0.775	2.160	21.615	0.877	1.237	29.210	0.904	0.261	15.588	0.443	20.054
SuperSloMo	13.387	0.749	2.980	—	—	—	28.756	0.893	0.270	15.657	0.471	19.757

Table 1: Metrics averaging over all 7 intermediate frames. We report the scores of the best-sampled sequences for SDVI.

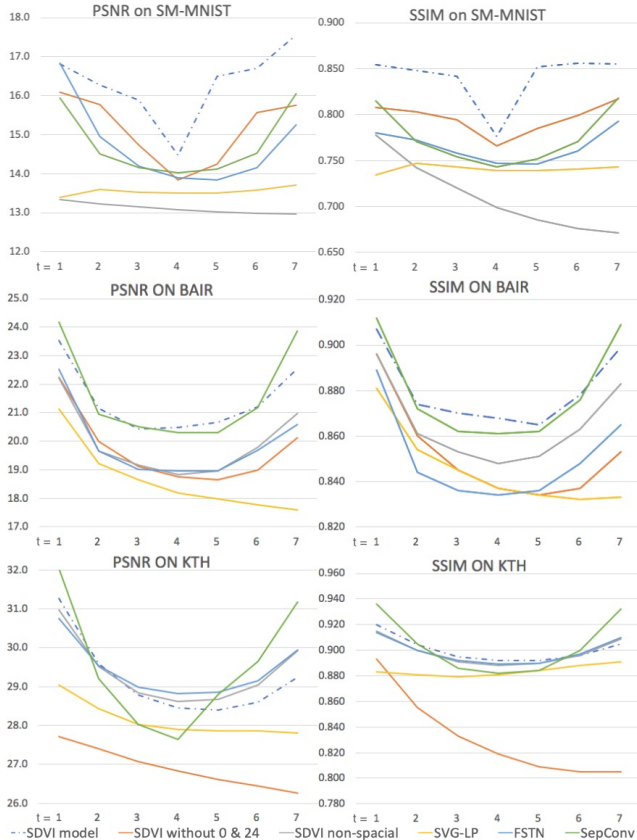


Figure 7: Average PSNR and SSIM at each step in test sets.

icant position differences, interpolation models such as SepConv and SuperSloMo would still choose to move the pixel based on the proximity between the two frames: the digits 2 and 5 gradually transfer to each other since the 2 in frame 8 is closer to the 5 in frame 16. Because the deterministic model FSTN cannot handle the uncertainties after a bounce, the model gets confused and generates a blurry result. The SVG-LP cannot converge in this setting since it doesn't have a constraint planning module like the *RBCConvLSTM* to lead the sequence to the final frame. Without spatial independence, a non-spatial representation cannot sample different dynamics for different areas. The two digits in the result of "SDVI non-spatial" collapse into one, then move

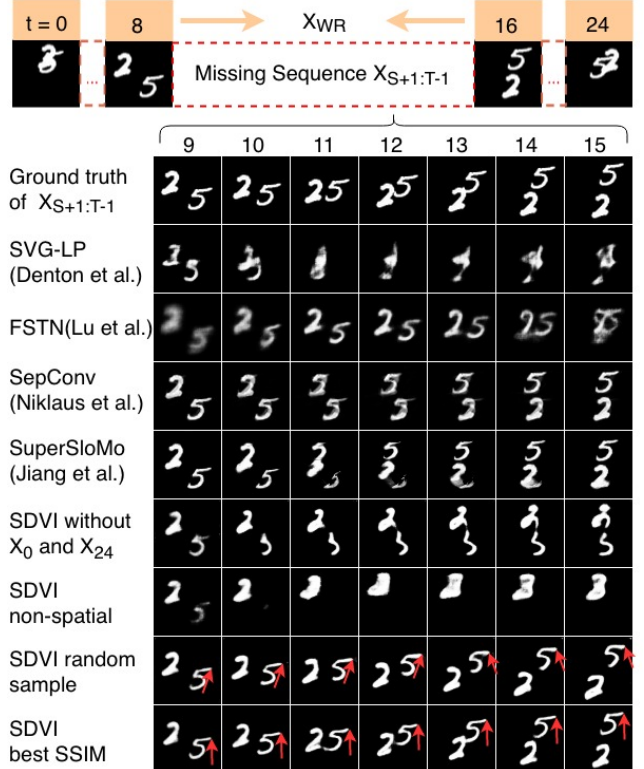


Figure 8: The digit 5 in our best sequence follows the upward trajectory of the ground truth. In another sampled sequence, the 5 goes upper right and then bounce upper left.

toward the final frame. Finally, our full model can learn the bouncing rule and provide plausible alternative sequences. Although our randomly sampled sequence diverges from the ground truth, this sequence can still keep the coherency with frame 8 and 16 under plausible dynamics.

We also study how good our method models the uncertainty as in (Denton and Fergus 2018). In 768 test sequences, we randomly select two digits for each sequence and synchronize all sequences' trajectories. Figure 9 shows the normalized average variance of the distribution of z_t for frames 2 to 14 (generated), while frame 1 and 15 are the ground truth.

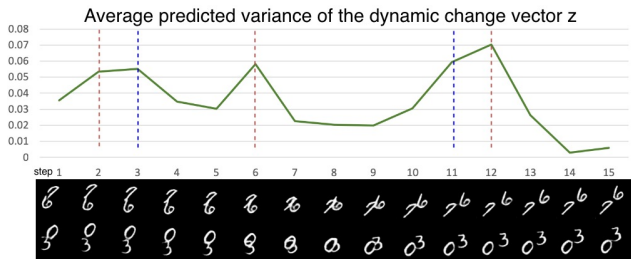


Figure 9: SDVI generates higher variances coincident to the "wall bouncing" event, indicated by the two dash lines (e.g. first sequence: red lines mark the bounces of the digit 6 and blue ones mark the bounces of 7).

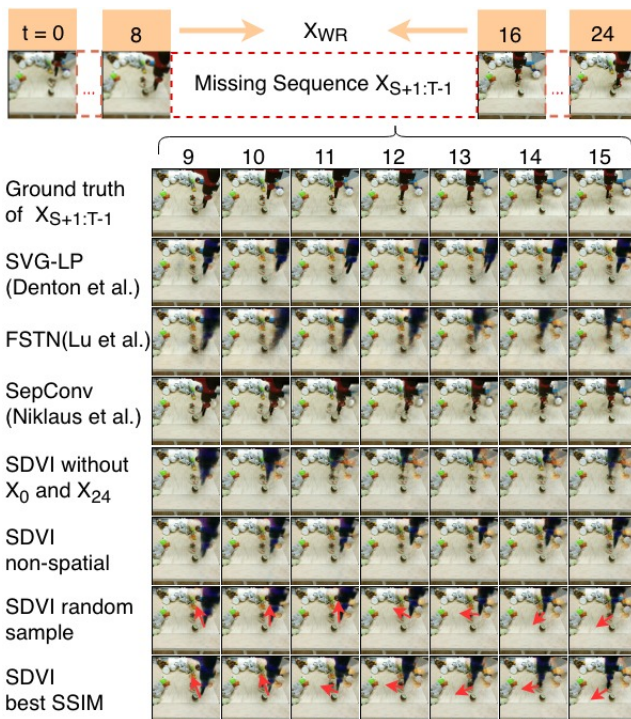


Figure 10: The arm in the best sequence follows the same movements in ground truth: first upward left then downward left. In another sampled sequence, the arm firstly goes straight up and then straight left, finally downward left.

BAIR robot pushing dataset

The BAIR robot pushing dataset (Ebert et al. 2017) contains sequences of a robot arm pushing various objects in the RGB domain. The movements of the arm don't follow smooth trajectories, and the movement changes are prompt. As shown in Table 1, although our SDVI marginally outperforms other models on SSIM, the SepConv achieves the best PSNR. As shown in Figure 10, since the SepConv relies more on pixel proximity, the shapes of the static objects in this method are nicely preserved. However, SepConv can't model the stochasticity while its movement is simplified to a straight sliding. The frames in the middle suffer the most

in all metrics (Figure 7). The stochasticity of the movement makes it hard for SVG-LP's arm to go back to the final frame and for FSTN to generate sharp shapes. The objects created by SDVI without spatial sampling are more blurry since all the areas will be disturbed by the dynamics change. On the other hand, the result of SDVI without using the reference frames 0 and 24 diverges too much away from the ground truth movement. Our full model cannot only sample a similar sequence to the ground truth, but sequences with reasonably varied movements (last two rows in Figure 10).

KTH Action Dataset

The KTH Action dataset (Schuldt, Laptev, and Caputo 2004) contains real-world videos of multiple human actions. Although the background is uniform, there is still some pixel noise. We found setting the mask's weight to 5 on moving pixels and 0 on noise is beneficial. Since most actions such as waving follow fixed patterns, the FSTN and the SepConv can achieve the best scores in PSNR and SSIM (Table 1). However, if the object in frame 8 and 16 has a similar body pose, the SepConv and the SuperSloMo will freeze the object's body and slide the object to its new position (Figure 13). SDVI without frame 0 and 24 suffers from the uncertainties of the initial state (Figure 13). Illustrated in Figure 12, the result of FSTN contains blurry pixels on moving region although it keeps the static parts sharp. Our sequence with best SSIM has a similar pattern as the ground truth. Even the random sampled sequence shown in Figure 12 has different dynamics in the middle, its initial and final movements still stick to the ground truth. Therefore our model still achieves an outstanding LMS over other methods (Table 1).

UCF101

Collected from YouTube, UCF101 contains realistic human actions captured under various camera conditions. We train both our model and SepConv on the training set of UCF101, and we get the result from the authors of (Jiang et al. 2017). Our results over 557 test videos outperform both SepConv and SuperSloMo (Table 1). In Figure 11, our model can infer the people's motion consistently. On the other hand, it's challenging for SepConv and SuperSloMo to estimate the pixel movement for the middle frames (frame 4 to 6), even they can generate sharper frames near the two reference frames.

Conclusions and Future Work

We have presented a stochastic generation framework SDVI that can infill long-term video intervals. To the best of our knowledge, it is the first study using extended reference frames and using a stochastic generation model to infill long intervals in videos. Three modules are introduced to sample a plausible sequence that preserves the consistency and the movement variety. Extensive ablation studies and comparisons with state-of-the-art methods demonstrate our good performance on 4 datasets. A metric LMS is proposed to evaluate the sequence coherency. Although currently SDVI can be iteratively applied to infill a interval with any numbers of frames, its flexibility could be further improved. An-

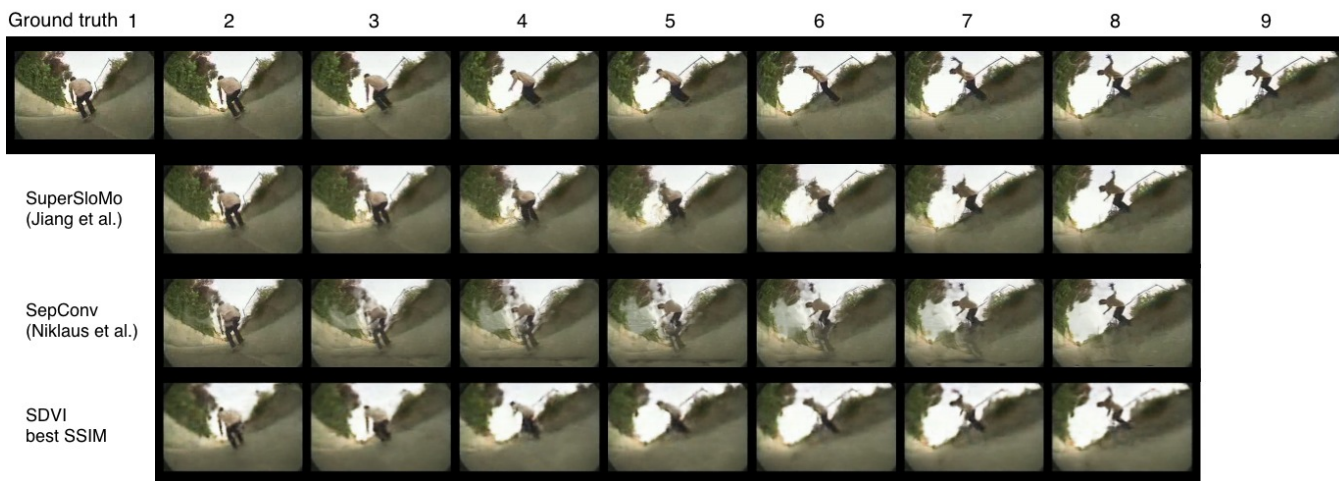


Figure 11: Best view in color. See Appendix E in the supplemental material for more comparisons on UCF101.

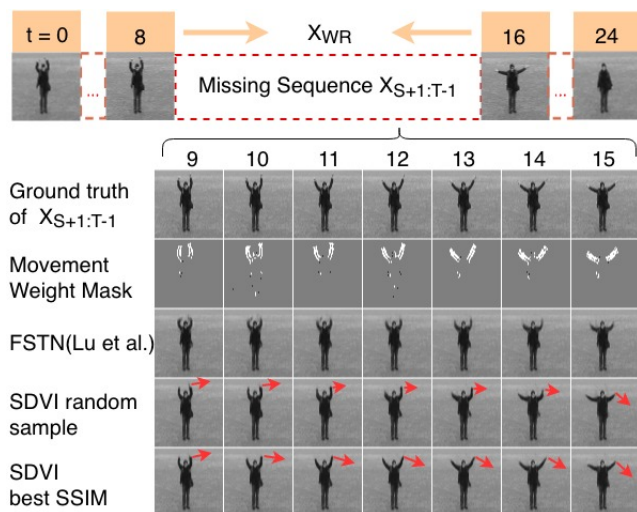


Figure 12: Our best-sampled sequence keeps the arm straight. In a randomly sampled sequence, the forearm bends first then stretches straight in the end. See the full comparison in Appendix E in the supplemental material.

other direction is to enhance the generality of the model to work across different video domains.

References

[Babaeizadeh et al. 2017] Babaeizadeh, M.; Finn, C.; Erhan, D.; Campbell, R. H.; and Levine, S. 2017. Stochastic variational video prediction. *arXiv preprint arXiv:1710.11252*.

[Cai et al. 2017] Cai, H.; Bai, C.; Tai, Y.-W.; and Tang, C.-K. 2017. Deep video generation, prediction and completion of human action sequences. *arXiv preprint arXiv:1711.08682*.

[Denton and Fergus 2018] Denton, E., and Fergus, R. 2018. Stochastic video generation with a learned prior. *arXiv preprint arXiv:1802.07687*.

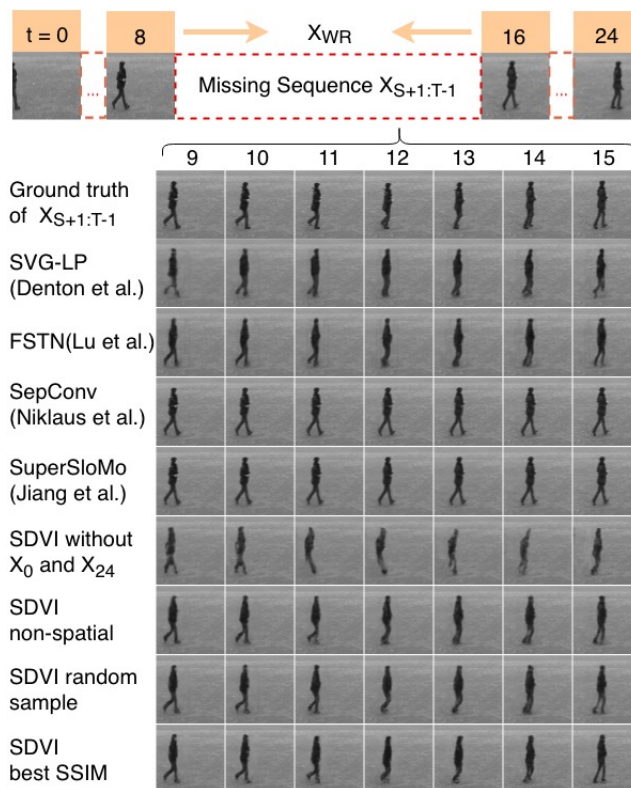


Figure 13: The sliding tendency of SepConv will cause motion errors and high LMS.

[Denton and others 2017] Denton, E. L., et al. 2017. Unsupervised learning of disentangled representations from video. In *Advances in Neural Information Processing Systems*, 4414–4423.

[Ebert et al. 2017] Ebert, F.; Finn, C.; Lee, A. X.; and Levine, S. 2017. Self-supervised visual planning with temporal skip connections. *arXiv preprint arXiv:1710.05268*.

- [Finn, Goodfellow, and Levine 2016] Finn, C.; Goodfellow, I.; and Levine, S. 2016. Unsupervised learning for physical interaction through video prediction. In *Advances in neural information processing systems*, 64–72.
- [Fox and Roberts 2012] Fox, C. W., and Roberts, S. J. 2012. A tutorial on variational bayesian inference. *Artificial intelligence review* 38(2):85–95.
- [Goodfellow et al. 2014] Goodfellow, I.; Pouget-Abadie, J.; Mirza, M.; Xu, B.; Warde-Farley, D.; Ozair, S.; Courville, A.; and Bengio, Y. 2014. Generative adversarial nets. In *Advances in neural information processing systems*, 2672–2680.
- [He et al. 2015] He, K.; Zhang, X.; Ren, S.; and Sun, J. 2015. Deep residual learning for image recognition. corr. vol. abs/1512.03385.
- [Henaff, Zhao, and LeCun 2017] Henaff, M.; Zhao, J.; and LeCun, Y. 2017. Prediction under uncertainty with error-encoding networks. *arXiv preprint arXiv:1711.04994*.
- [Herbst, Seitz, and Baker 2009] Herbst, E.; Seitz, S.; and Baker, S. 2009. Occlusion reasoning for temporal interpolation using optical flow. *Department of Computer Science and Engineering, University of Washington, Tech. Rep. UW-CSE-09-08-01*.
- [Ilg et al. 2017] Ilg, E.; Mayer, N.; Saikia, T.; Keuper, M.; Dosovitskiy, A.; and Brox, T. 2017. FlowNet 2.0: Evolution of optical flow estimation with deep networks. In *IEEE conference on computer vision and pattern recognition (CVPR)*, volume 2, 6.
- [Jiang et al. 2017] Jiang, H.; Sun, D.; Jampani, V.; Yang, M.-H.; Learned-Miller, E.; and Kautz, J. 2017. Super slomo: High quality estimation of multiple intermediate frames for video interpolation. *arXiv preprint arXiv:1712.00080*.
- [Kingma and Welling 2013] Kingma, D. P., and Welling, M. 2013. Auto-encoding variational bayes. *arXiv preprint arXiv:1312.6114*.
- [Lee et al. 2018] Lee, A. X.; Zhang, R.; Ebert, F.; Abbeel, P.; Finn, C.; and Levine, S. 2018. Stochastic adversarial video prediction. *arXiv preprint arXiv:1804.01523*.
- [Liu et al. 2017] Liu, Z.; Yeh, R. A.; Tang, X.; Liu, Y.; and Agarwala, A. 2017. Video frame synthesis using deep voxel flow. In *ICCV*, 4473–4481.
- [Lu, Hirsch, and Schölkopf 2017] Lu, C.; Hirsch, M.; and Schölkopf, B. 2017. Flexible spatio-temporal networks for video prediction. In *Proceedings of the IEEE Conference on Computer Vision and Pattern Recognition*, 6523–6531.
- [Mathieu, Couprie, and LeCun 2015] Mathieu, M.; Couprie, C.; and LeCun, Y. 2015. Deep multi-scale video prediction beyond mean square error. *arXiv preprint arXiv:1511.05440*.
- [Meyer et al. 2015] Meyer, S.; Wang, O.; Zimmer, H.; Grosse, M.; and Sorkine-Hornung, A. 2015. Phase-based frame interpolation for video. In *Proceedings of the IEEE Conference on Computer Vision and Pattern Recognition*, 1410–1418.
- [Meyer et al. 2018] Meyer, S.; Djelouah, A.; McWilliams, B.; Sorkine-Hornung, A.; Gross, M.; and Schroers, C. 2018. Phasenet for video frame interpolation. In *Proceedings of the IEEE Conference on Computer Vision and Pattern Recognition*, 498–507.
- [Niklaus and Liu 2018] Niklaus, S., and Liu, F. 2018. Context-aware synthesis for video frame interpolation. *arXiv preprint arXiv:1803.10967*.
- [Niklaus, Mai, and Liu 2017a] Niklaus, S.; Mai, L.; and Liu, F. 2017a. Video frame interpolation via adaptive convolution. In *IEEE Conference on Computer Vision and Pattern Recognition*, volume 1, 3.
- [Niklaus, Mai, and Liu 2017b] Niklaus, S.; Mai, L.; and Liu, F. 2017b. Video frame interpolation via adaptive separable convolution. *CoRR* abs/1708.01692.
- [Schuldt, Laptev, and Caputo 2004] Schuldt, C.; Laptev, I.; and Caputo, B. 2004. Recognizing human actions: a local svm approach. In *Pattern Recognition, 2004. ICPR 2004. Proceedings of the 17th International Conference on*, volume 3, 32–36. IEEE.
- [Srivastava, Mansimov, and Salakhudinov 2015] Srivastava, N.; Mansimov, E.; and Salakhudinov, R. 2015. Unsupervised learning of video representations using lstms. In *International conference on machine learning*, 843–852.
- [Tulyakov et al. 2017] Tulyakov, S.; Liu, M.-Y.; Yang, X.; and Kautz, J. 2017. Mocogan: Decomposing motion and content for video generation. *arXiv preprint arXiv:1707.04993*.
- [Villegas et al. 2017] Villegas, R.; Yang, J.; Hong, S.; Lin, X.; and Lee, H. 2017. Decomposing motion and content for natural video sequence prediction. *arXiv preprint arXiv:1706.08033*.
- [Vondrick, Pirsivash, and Torralba 2016] Vondrick, C.; Pirsivash, H.; and Torralba, A. 2016. Generating videos with scene dynamics. In *Advances In Neural Information Processing Systems*, 613–621.
- [Wichers et al. 2018] Wichers, N.; Villegas, R.; Erhan, D.; and Lee, H. 2018. Hierarchical long-term video prediction without supervision. *arXiv preprint arXiv:1806.04768*.
- [Xingjian et al. 2015] Xingjian, S.; Chen, Z.; Wang, H.; Yeung, D.-Y.; Wong, W.-K.; and Woo, W.-c. 2015. Convolutional lstm network: A machine learning approach for precipitation nowcasting. In *Advances in neural information processing systems*, 802–810.
- [Yu et al. 2013] Yu, Z.; Li, H.; Wang, Z.; Hu, Z.; and Chen, C. W. 2013. Multi-level video frame interpolation: Exploiting the interaction among different levels. *IEEE Transactions on Circuits and Systems for Video Technology* 23(7):1235–1248.

Appendices

Proof of the sequence Variational Lower Bound

We can set $P(\tilde{X}_{S:T})$ as the probability of any sequence. The logarithm of this probability has the following variational

lower bound:

$$\log P(\tilde{X}_{S+1:T-1}) = \log \int_z P(\tilde{X}_{S+1:T-1}|z_{S:T-1}) P(z_{S:T-1}) \frac{Q(z_{S:T})}{Q(z_{S:T})} \quad (5)$$

$$= \log \mathbb{E}_{Q(z_{S:T})} \frac{P(\tilde{X}_{S+1:T-1}|z_{S:T-1}) P(z_{S:T})}{Q(z_{S:T})} \quad (6)$$

$$\geq \mathbb{E}_{Q(z_{S:T})} \frac{P(\tilde{X}_{S+1:T-1}|z_{S:T-1}) P(z_{S:T})}{Q(z_{S:T})} \quad (7)$$

$$= \mathbb{E}_{Q(z_{S:T})} \log P(\tilde{X}_{S+1:T-1}|z_{S:T-1}) - E_{Q(z_{S:T})} \frac{Q(z_{S:T})}{P(z_{S:T})} \quad (8)$$

$$= \mathbb{E}_{Q(z_{S:T})} \log \prod_t P(\tilde{X}_t|\tilde{X}_{S:t-1}, z_{S:t}) - \int_z Q(z_{S:T}) \log \frac{Q(z_{S:T})}{P(z_{S:T})} \quad (9)$$

$$= \sum_{t=S}^{T-1} \mathbb{E}_{Q(z_t)} \log P(\tilde{X}_t|\tilde{X}_{S:t-1}, z_{S:t}) - \int_z Q(z_{S:T}) \log \frac{Q(z_{S:T})}{P(z_{S:T})} \quad (10)$$

Deduction and reasoning details of the objective

Since we use the output from the inference section as the result during inference phase, we are mostly interested in maximizing $\log P(\tilde{X}_{S:T-1}^{infr})$. Since the lower bound shown in Appendix A will hold for any form of the distribution, we can fit P_{pst} and P_{infr} into (10)'s $P(z_{S:t})$ and $Q(z_{S:T})$:

$$\log P(\tilde{X}_{S:T-1}^{infr}) \geq \sum_{t=S}^{T-1} \left[\mathbb{E}_{P_{infr}(z_t)} \log P(X_t^{infr}|X_{S:t-1}^{infr}, z_{S:t}^{infr}) - \int_{z_{S:T-1}^{infr}} P_{infr} \cdot \log \frac{P_{infr}}{P_{pst}} \right] \quad (11)$$

The integration part (KL divergence of the sequence) in the above inequality can be decomposed as:

$$\begin{aligned} & \int_{z_{S:T-1}^{infr}} P_{infr} \cdot \log \frac{P_{infr}}{P_{pst}} \\ &= \int_{z_S^{infr}} \int_{z_{S+1}^{infr}} \dots \int_{z_{T-1}^{infr}} \left[\prod_{t=S}^T P_{infr}(z_t|X_{S:t-1}^{infr}, X_{WR}) \cdot \sum_t \log \frac{P_{infr}(z_t|X_{S:t-1}^{infr}, X_{WR})}{P_{pst}(z_t|X_{S:t}^{pst})} \right] \\ &= \sum_{t=1}^{T-1} \mathbb{E}_{P_{infr}(z_t|X_{S:t-1}^{infr}, X_{WR})} \log \frac{P_{infr}(z_t|X_{S:t-1}^{infr}, X_{WR})}{P_{pst}(z_t|X_{S:t}^{pst})} \quad (12) \\ &= \sum_{t=1}^{T-1} D_{KL}(P_{infr}(z_t|X_{S:t-1}^{infr}, X_{WR}) || P_{pst}(z_t|X_{S:t}^{pst})) \quad (14) \end{aligned}$$

Therefore if we put (14) back to the lower bound (11), the logarithm of the probability we want to maximize becomes:

$$\log P(\tilde{X}_{S:T-1}^{infr}) = \sum_{t=S}^{T-1} \left[\mathbb{E}_{P_{infr}(z_t)} \log P(X_t^{infr}|X_{S:t-1}^{infr}, z_{S:t}^{infr}) - D_{KL}(P_{infr}(z_t|X_{S:t-1}^{infr}, X_{WR}) || P_{pst}(z_t|X_{S:t}^{pst})) \right]$$

$$- D_{KL}(P_{infr}(z_t|X_{S:t-1}^{infr}, X_{WR}) || P_{pst}(z_t|X_{S:t}^{pst})) \quad (15)$$

Because the neural network sometimes has the tendency to use the easiest way to fit the objective, if we only maximize (15), the $LSTM_{GT}$ will ignore the information introduced by X_t . The $P_{infr}(z_t)$ and $P_{infr}(z_t)$ will degenerate to a convenient fixed value to lower the D_{KL} . Our Inference module and Posterior module then will resemble the SVG-FP, which is a simpler version of SVG-LP with fixed prior distribution.

To prevent the degeneration, we also need to maximize the probability of the reconstruction result \tilde{X}_t^{pst} to force the newly observed dynamic from X_t to be included in P_{pst} . Here we fit P_{infr} and P_{pst} into (10)'s $P(z_{S:t})$ and $Q(z_{S:t})$ and we end up also maximizing:

$$\begin{aligned} \log P(\tilde{X}_{S:T-1}^{pst}) &= \sum_{t=S}^{T-1} \left[\mathbb{E}_{P_{pst}(z_t)} \log P(X_t^{pst}|X_{S:t-1}^{pst}, z_{S:t}^{pst}) \right. \\ &\quad \left. - D_{KL}(P_{pst}(z_t|X_{S:t-1}^{pst}) || P_{infr}(z_t|X_{S:t-1}^{infr}, X_{WR})) \right] \quad (16) \end{aligned}$$

The deduction process of this result is the same as the transformation from (11) to (15). Finally, we design a objective function to maximize both of (15) and (16) at the same time.

Architecture and Training Details

The *Encoder*, the *Extractor* and the *Decoder* use the same architecture of DCGAN. For step S and T , feature maps of all layers in *Encoder* will be gathered as a multi-scale residuals ctn_S and ctn_T to help reconstruct the static content. The $LSTM_{infr}$, the $LSTM_{pst}$ and the $LSTM_{dyn}$ use the structure of one layer ConvLSTM. The output dimensions of our modules are listed in Table 2. Our reported result is created using one extended references frame on each side (totally 2 extended reference frames). These two extra references bring extra long-term information into the Reference module. However, frames too far away from the interval would contain too much unrelated information. We also tested on 4 extended reference frames and find the benefit is insignificant.

For the evaluation presented in our paper, all datasets have been trained with a input frame dimension of 64×64 with a interval of 7 frames. We also train on KTH with a input frame dimension of 128×128 (See Section 2 in the video web page) and BAIR with intervals of 9 frames (See Section 1 in the video web page). We use standard Adam optimizer with 0.5 as the first momentum decay rate. All settings of the hyper parameters for different datasets are shown in 3. The β is initially set to 1 and gradually reduce to 0.4. To prevent the accumulation of errors, we will first roll back the cell state of $LSTM_{infr}$ to $t-1$, and then input h_t after inferring the $N_{infr}(\mu_t, \sigma_t)$. This operation has been proved to be crucial to our result. On the early stage of the training, a less meaningful \hat{h}_t would accumulatively disturb the cell state of $LSTM_{infr}$ and lead to a slow convergence.

Dataset Details

SMMNIST: Sequences were generated on the fly by randomly choosing two digits from MNIST: 50k digits from MNIST training set for training, 10k digits for validation,

Feature	Dim 1	Dim 2	Dim 3
C_{start}	4	4	256
C_{end}	4	4	256
h_t	4	4	256
\hat{h}_t	4	4	256
σ_t SMMNIST & KTH	4	4	32
μ_t SMMNIST & KTH	4	4	32
σ_t BAIR	4	4	64
μ_t BAIR	4	4	64

Table 2: The dimensionalities of different features

Training Parameters	SMMNIST	BAIR	KTH
α	0.002	0.0002	0.0002
γ	0.001	0.0001	0.0001
β	1 to 0.4	1 to 0.4	1 to 0.4
Mask Weight η	N/A	2	5

Table 3: Hyper parameters for training on different datasets

and 10k in MNIST testing set for testing. We create the ground truth video frames as 16 fps.

KTH: We used person 1-14 (1337vids) for training, 15-16(190vids) for validation and 17-25 (863vids) for testing. We sample the ground truth video frames as 12 fps.

Bair: By default, we use 40000 scenes for training, 3863 for validation and 256 for testing. We sample the ground truth video frames as 16 fps.

UCF101: The dataset contains 101 realistic human actions taken in a wild and exhibits various challenges, such as background clutter, occlusion, and complicated motion. The training set contains 3223 video sequences with varying length, and the test set contains 557 video sequences. We sample the video as 16 fps so that the input reference frames for the network are 2 fps.

More Results

Figure 15 shows the full comparisons of the wave action and Figure 16 provides another UCF101 comparison. Results of more conditions and more promising results can be found in the “video_result.html”. Please open the webpage in your browser to see (the web page contains gif videos such as: Figure 14).

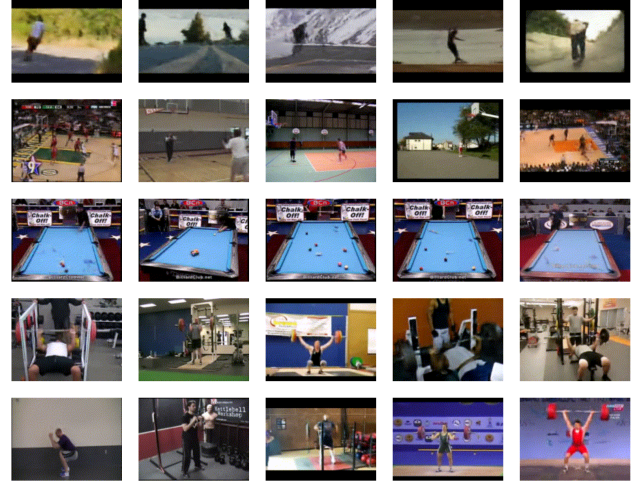


Figure 14: a snapshot of the gifs in the “video_result.html”

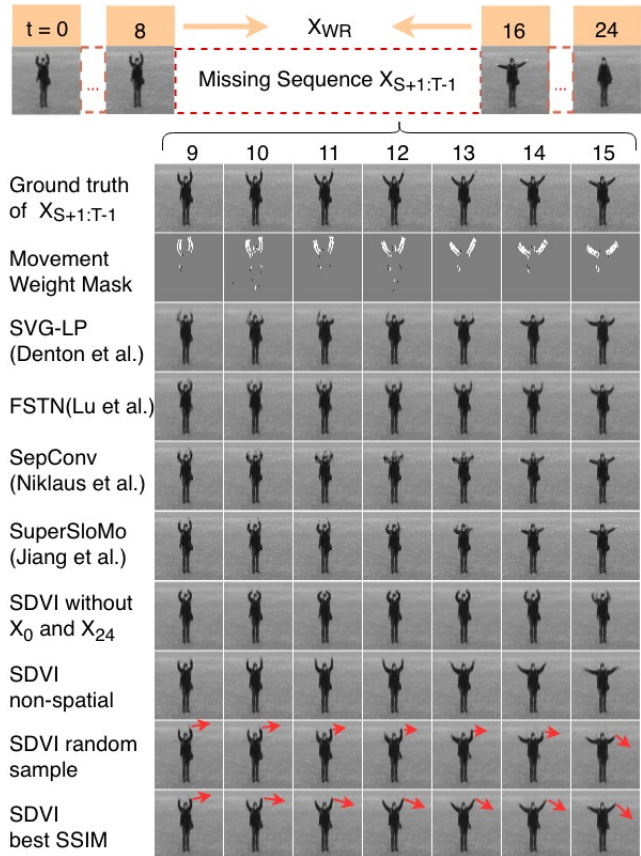


Figure 15: shows the full comparisons for he wave action. We also show another comparison result of our model with SepConv and SuperSloMo in Figure

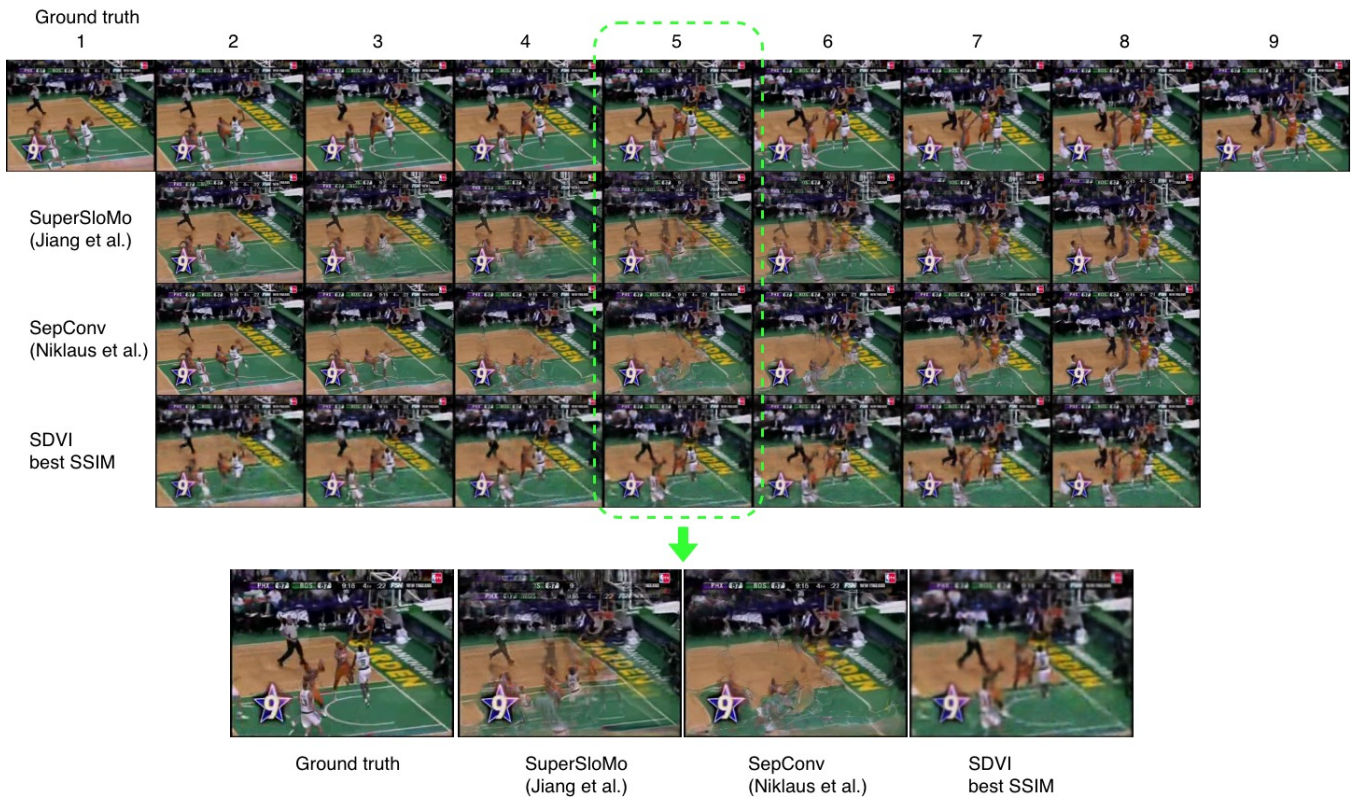


Figure 16: A more complicated UCF101 example: a real basketball video sequence involving multiple objects. Our method can model the dynamic correctly and generate better moving objects than SuperSloMo and SepConv.